

# Harmonic Closed-Loop Model Combined Predictive Fault-Tolerant Control of Double Parallel Rotor Permanent Magnet Synchronous Motor

Hai Pu\*

*Architecture Engineering School, Chongqing Industry & Trade Polytechnic, Chongqing 408000, China*

**ABSTRACT:** Double Parallel Rotor Permanent Magnet Synchronous Motors exhibit superior performance and compact size, but the growing trend of electrification imposes higher demands on them. This study proposes a predictive fault-tolerant control integrating a closed-loop identification model and conducts experiments on Double Parallel Rotor Permanent Magnet Synchronous Motors. Results indicated that the proposed closed-loop identification model, along with its fractional-order lead-lag compensator module, effectively optimized motor performance, reducing average tracking error by 78.36%. Additionally, with demagnetization faults, the predictive fault-tolerant control outperformed traditional fault-tolerant control in speed, current, and torque fault-tolerant control, demonstrating superior performance. Through 10 weeks of practical application records, Double Parallel Rotor Permanent Magnet Synchronous Motors achieved a working accuracy of 95%–99% under the closed-loop identification model, with recall rates reaching 92%–96% in fault-tolerant scenarios. In both natural and simulated demagnetization fault situations, 97.69% of Double Parallel Rotor Permanent Magnet Synchronous Motors could continue normal operation. This research holds positive significance for the development of motor systems and enhancing their adaptability in the trend of electrification.

## 1. INTRODUCTION

In today's industrial and transportation sectors, the performance of motor systems is crucial for improving energy efficiency and achieving intelligent production [1]. As an advanced structure in motor systems, Double Parallel Rotor Permanent Magnet Synchronous Motor (DRPMSM) has attracted widespread research interest due to its unique design and outstanding performance [2]. However, as motor systems continue to evolve and become more complex, the need to enhance their robustness, reliability, and control precision has become increasingly urgent [3]. In practical operation, motor systems often face challenges from various aspects, including nonlinear characteristics, load disturbances, external interference, and performance degradation caused by harmonics within the system [4]. Especially in high-precision and demanding applications such as precision instrument manufacturing, electric vehicle propulsion, and aerospace, the issues posed by these challenges require higher stability and accuracy from motor systems [5, 6]. Traditional closed-loop control strategies have struggled to meet the growing demands of the system. Therefore, this study proposes a DRPMSM harmonic closed-loop model integrating a closed-loop identification model. The model analyzes the error magnitude characteristics in the motor, enhances DRPMSM identification accuracy through the closed-loop identification model, and achieves predictive fault-tolerant control. The research aims to improve the performance of DRPMSM systems, providing a novel and ef-

ficient solution for intelligent control and uncertainty response in motor systems through a comprehensive control framework.

The research is mainly divided into four parts. The first part introduces the current research on DRPMSM and its performance optimization, fault-tolerant control, etc. The second part establishes the mathematical model of DRPMSM and explains the prediction error control method based on the closed-loop identification model. The third part conducts experiment on the proposed predictive fault-tolerant control to verify its effectiveness and feasibility. The final section summarizes the entire research content, points out the research shortcomings, and provides prospects.

## 2. RESEARCH BACKGROUNDS

DRPMSM is a motor design structure that consists of two rotors. Introducing new design concepts and structures has brought more possibilities and innovations to the field of motor technology [7]. Ladghem-Chikouche and the team proposed a two-dimensional hybrid model for solving the magnetic field distribution of dual-rotor permanent magnet synchronous motors. This model was based on the precise subdomain technique and finite difference method, addressing the common modeling challenges in motor design considering nonlinearity and magnetic saturation effects. This approach aimed to enhance the computational efficiency and accuracy of results [8]. In addressing the issue of low internal space utilization in single-rotor motors, Wu and his colleagues designed four different dual-rotor permanent magnet synchronous motors. They com-

\* Corresponding author: Hai Pu (ph\_cqfl@163.com).

pared their performance, including air gap flux density, electromagnetic field, torque characteristics, efficiency, etc. They used the equivalent magnetic circuit method and finite element analysis. This comparison provided guidance for rotor structure selection [9]. To meet the demand for improving motor torque density and output characteristics, Ghaffarpour and Mirsalim proposed an innovative dual-rotor permanent magnet switched reluctance motor. Through tooth segmentation design, the motor's torque density was increased, and the introduction of a small permanent magnet generator between stator poles improved output characteristics. This offered a practical design and validation method for innovative motor structures [10]. Alahyari and Torkaman addressed the need to enhance the performance of a cursor mechanical system by proposing a bidirectional pole dual-rotor permanent magnet cursor mechanical system composed of double-sided stators, windings, and inner and outer slot magnets. This system demonstrated superior performance in terms of magnetic flux, torque, power factor, and notably, torque density compared to traditional virtual machines [11].

The optimization of the performance of Permanent Magnet Synchronous Motors involves various aspects, including mechanical structure, electromagnetic design, and control strategies. Fault-tolerant control for Permanent Magnet Synchronous Motors is a technique aimed at improving system reliability and robustness, with the goal of maintaining normal operation when the motor experiences faults or abnormal conditions. Sun et al. addressed control issues in bearingless Permanent Magnet Synchronous Motor drives and proposed an optimization control strategy based on the Grey Wolf Optimization algorithm for state feedback control. This strategy exhibited faster response times and no overshoot compared to traditional controllers, effectively optimizing the design of Permanent Magnet Synchronous Motor drives [12]. Fang et al. tackled the optimization of controller parameters in Permanent Magnet Synchronous Motors, introducing a parameter adjustment design model based on an improved hybrid particle swarm optimization algorithm. Through the algorithm, they optimized the parameters controlling speed and position in Permanent Magnet Synchronous Motors, significantly enhancing the performance of the motors [13]. Zuo et al. addressed the low fault tolerance of dual-inverter-fed open-winding Permanent Magnet Synchronous Motors, presenting a fault-tolerant control method based on winding reconnection. This approach improved the fault tolerance of Permanent Magnet Synchronous Motors against multiple open-circuit faults, providing a new solution for their application in electric vehicles [14]. Jlassi and Cardoso focused on the problem of back-to-back converter failures in Permanent Magnet Synchronous Motor drives, proposing an efficient model predictive fault-tolerant current control algorithm. This algorithm aimed to enhance the reliability and availability of wind turbines powered by Permanent Magnet Synchronous Motors [15].

In summary, the introduction of DRPMSM and various innovative design structures has brought new possibilities to the field of motor technology. Performance optimization and fault-tolerant control, as essential means to improve the reliability and robustness of Permanent Magnet Synchronous Motor sys-

tems, have been widely researched and applied. However, there is limited research discussing the application of closed-loop identification models in DRPMSMs. Therefore, investigating fault-tolerant control strategies by combining closed-loop identification models and harmonic closed-loop models holds the potential for breakthroughs in enhancing the performance and fault tolerance of Permanent Magnet Synchronous Motor systems.

### 3. FAULT-TOLERANT CONTROL OF HARMONIC CLOSED-LOOP MODEL FOR DRPMSM BASED ON CLOSED-LOOP IDENTIFICATION MODEL

This section provides a brief overview of DRPMSM and then focuses on the harmonic closed-loop model of DRPMSM, integrating the closed-loop identification model for modeling purposes. After obtaining its mathematical model, the section elaborates on feedback control based on closed-loop identification and predictive fault-tolerant control, thus completing a detailed introduction to the research methodology.

#### 3.1. Modeling of DRPMSM Harmonic Closed-Loop Control with Integrated Closed-Loop Identification Model

DRPMSM and single-rotor permanent magnet synchronous motors exhibit significant differences in structure and performance. Single-rotor permanent magnet synchronous motors have a simple structure and are suitable for applications with general performance and power density requirements, such as household appliances and general industrial drives [16, 17]. In contrast, DRPMSM, by introducing two rotating rotors, provides higher power density and performance within the same volume, which makes it suitable for areas with higher power density requirements, such as high-performance electric vehicles and wind power generation [18]. The schematic diagram of the DRPMSM structure is shown in Figure 1.

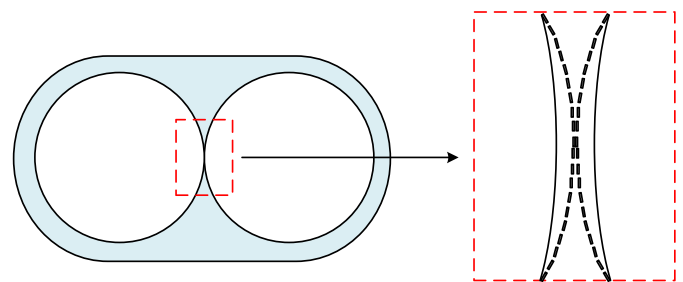


FIGURE 1. Schematic diagram of the internal structure of DRPMSM.

From Figure 1, it can be observed that DRPMSM typically consists of two independent rotors, each with its stator. These two rotors are usually located on the same axis and can share the same rotating axis or adjacent axes. Each rotor can be considered as an independent motor unit with its own stator and permanent magnet. The harmonic closed-loop model of DRPMSM refers to the use of a harmonic closed-loop model to describe its operation and control characteristics in a dual-rotor structure of a permanent magnet synchronous motor. The harmonic closed-loop model is a mathematical model used to

analyze and control harmonic effects in motor systems. In permanent magnet synchronous motors, there may be harmonic components in current and magnetic fields that affect the performance and efficiency of the motor. However, the dual-rotor structure makes the mathematical model of the motor system more complex, especially when considering harmonics and nonlinear effects, increasing the difficulty of modeling and controlling the system. Additionally, compared to ordinary single-rotor permanent magnet synchronous motors, the DRPMSM structure is more complex, and its tracking accuracy and stability decrease continuously as the motor operates. Therefore, the study aims to achieve closed-loop identification of DRPMSM through current loop control, thereby reducing the impact of external interference signals on system parameter identification and improving the accuracy of identification. The purpose of integrating the closed-loop identification model is to adaptively estimate and adjust system parameters in real time to enhance adaptability to the complexity and uncertainty of the motor. The study initially establishes the mathematical model of DRPMSM in the rotor coordinate system, as shown in Equation (1).

$$\begin{cases} u_d = R_s i_d + L_d \left( \frac{di_d}{dt} \right) - \omega L_q i_q \\ u_q = \omega L_d i_d + L_q \left( \frac{di_q}{dt} \right) + R_s i_q + \omega \psi_f \\ F_{em} = \frac{3p_n \pi \psi_f i_q}{2\tau} = F_L + m \left( \frac{dv}{dt} \right) + Bv \end{cases} \quad (1)$$

In Equation (1),  $u_d$ ,  $u_q$ , and  $F_{em}$  represent the control voltage and electromagnetic thrust of the motor on the  $d$  and  $q$  axes, respectively;  $R_s$  denotes the stator resistance of the motor;  $i_d$  and  $i_q$  indicate the control currents on the  $d$  and  $q$  axes;  $L_d$  and  $L_q$  represent the inductance on the  $d$  and  $q$  axes;  $\omega$  is the angular velocity of the motor;  $\psi_f$  is the magnetic flux of the motor;  $p_n$  is the pole pair number;  $\tau$  is the motor's pole pair inductance time constant;  $F_L$  represents the load force;  $m$  represents the mass of the load;  $B$  is the damping of the load; and  $v$  is the velocity of the load. To simplify the control system, the study focuses on keeping the  $i_d$  value at 0, and  $u_q$  is shown in Equation (2).

$$u_q = L_q \left( \frac{di_q}{dt} \right) + R_s i_q + \omega \psi_f \quad (2)$$

Equation (2) is substituted into Equation (1) with a Laplace transform, which yields the transfer function model of the DRPMSM motion system from control voltage to velocity, as shown in Equation (3).

$$G(s) = \frac{v}{u_q} = \frac{3p_n \pi \psi_f - 2\tau F_L (L_q s + R_s)}{2\tau (L_q s + R_s) (ms + B) + 3\tau p_n \psi_f^2 - \frac{2\tau^2 \psi_f F_L (L_q s + R_s)}{\pi}} \quad (3)$$

In Equation (3),  $s$  is the complex variable of the transfer function, typically representing the complex frequency in the frequency domain. After simplification, the open-loop identification model transfer function of DRPMSM is obtained, as shown in Equation (4).

$$G(s) = \frac{b_1 s + b_0}{a_2 s^2 + a_1 s + a_0} \quad (4)$$

The terms  $b_1$ ,  $b_0$ ,  $a_0$ ,  $a_1$ ,  $a_2$  in Equation (4) are derived from Equation (3). They are detailed in Equation (5).

$$\begin{cases} b_1 = 3p_n \pi \psi_f - 2\tau F_L R_s \\ b_0 = 2\tau F_L L_q \\ a_0 = 2\tau B R_s + 3\tau p_n \psi_f^2 - \frac{2\tau^2 \psi_f F_L R_s}{\pi} \\ a_1 = 2\tau B L_q + 2\tau m R_s - \frac{2\tau^2 \psi_f F_L L_q}{\pi} \\ a_2 = 2\tau m L_q \end{cases} \quad (5)$$

In Equation (5),  $b_1$ ,  $b_0$ ,  $a_0$ ,  $a_1$ , and  $a_2$  are parameters to be identified. The denominator polynomial of this transfer function has a maximum order of 2, and the numerator polynomial has a maximum order of 1, making it a model with a double pole and a single zero. The constructed identification model accurately reflects the dynamic characteristics of the system while reducing the computational and experimental costs required for identification, thus enhancing efficiency. Building upon the open-loop identification model, the study introduces a proportional-integral (PI) closed-loop feedback controller for the current loop to transform the model into a closed-loop identification model. The goal of the PI controller is to minimize current errors by adjusting the control output, enabling the motor current to accurately follow the given current reference value, as shown in Equation (6).

$$C_1(s) = \frac{k_P s + k_I}{s} \quad (6)$$

In Equation (6),  $C_1(s)$  is the transfer function of the current loop, with  $k_P$  and  $k_I$  representing the proportional gain and integral gain, respectively. The closed-loop identification model block diagram of the DRPMSM with the added controller is illustrated in Figure 2.

The block diagram shown in Figure 2 improves the accuracy of control signal tracking. However, it inevitably alters the identification structure of the system. Therefore, when performing parameter identification, it is necessary to adjust the corresponding transfer functions to account for the influence of the current loop, ensuring the accuracy of parameter identification. The transfer function of the closed-loop identification model established based on Figure 2 is shown in Equation (7).

$$G'(s) = \frac{M(s)}{L(s) s + \left[ \frac{2\tau}{3p_n \pi \psi_f} + F_L \right] N(s)} \quad (7)$$

In Equation (7),  $L(s)$  represents the denominator polynomial of the closed-loop identification model, while  $M(s)$  and  $N(s)$  are the two components of the transfer function, as detailed in Equation (8).

$$\begin{cases} L(s) = 2\tau (L_q s + R_s) (ms + B) + 3\tau p_n \psi_f^2 - \frac{2\tau^2 \psi_f F_L (L_q s + R_s)}{\pi} \\ M(s) = (k_P s + k_I) [3p_n \pi \psi_f - 2\tau F_L (L_q s + R_s)] \\ N(s) = (ms + B) (k_P s + k_I) [3p_n \pi \psi_f - 2\tau F_L (L_q s + R_s)] \end{cases} \quad (8)$$

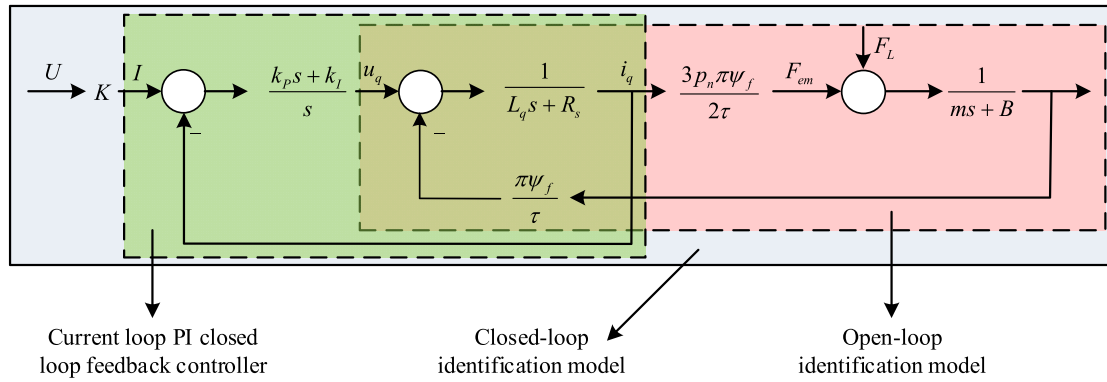


FIGURE 2. Closed-loop identification model of DRPMSM.

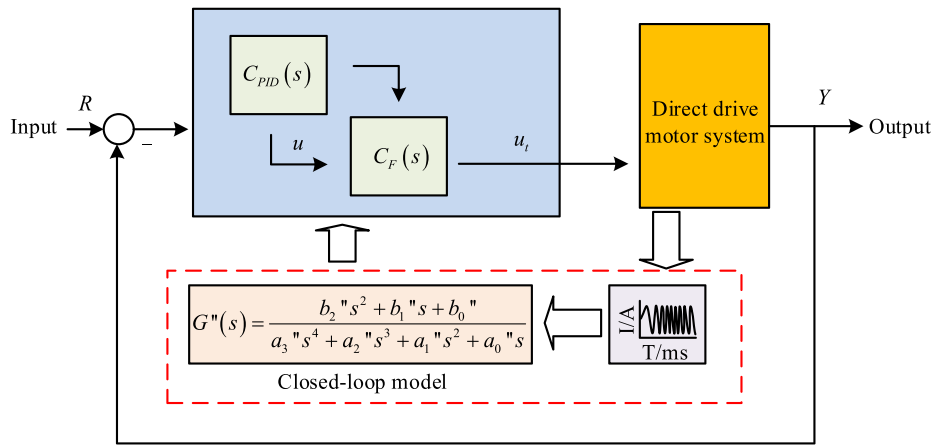


FIGURE 3. Fractional order feedback control method based on closed-loop identification model.

Equation (8) is arranged to yield the standard form of the transfer function; therefore, Equation (9) is obtained.

$$G'(s) = \frac{b'_2 s^2 + b'_1 s + b'_0}{a'_3 s^3 + a'_2 s^2 + a'_1 s + a'_0} \quad (9)$$

In Equation (9),  $b'_2, b'_1, b'_0,$  and  $a'_3, a'_2, a'_1, a'_0$  are parameters to be identified for closed-loop identification. The numerator polynomial of this transfer function has a maximum order of 2, and the denominator polynomial has a maximum order of 3, representing a model of a double pole triple-order system. At this point, the control voltage to displacement transfer function model of the DRPMSM motion system is given by Equation (10).

$$G''(s) = \frac{b''_2 s^2 + b''_1 s + b''_0}{a''_3 s^4 + a''_2 s^3 + a''_1 s^2 + a''_0 s} \quad (10)$$

In Equation (10), the denominator has an additional order compared to the closed-loop identification model, mainly reflecting the integration relationship between velocity and displacement. This additional order ensures a more comprehensive description of the dynamic characteristics of the system.

### 3.2. Feedback Control and Predictive Fault-Tolerant Control Based on Closed-Loop Identification

To further optimize the DRPMSM and achieve better performance metrics including system stability, response speed, and robustness, the research conducts a fractional-order feedback control method based on closed-loop identification models. The advantage of this approach lies in its better adaptation to the actual dynamic characteristics of the system. By more accurately modeling the system dynamics and employing the flexibility of a fractional-order controller, the DRPMSM can better adapt to different operating conditions and abnormal situations. Additionally, this approach helps improve the system's fault tolerance performance when facing faults or changes, demonstrating significant advantages in predictive fault-tolerant control. The specific fractional-order feedback control method is illustrated in Figure 3.

In Figure 3,  $R$  and  $Y$  represent the reference displacement and output displacement, while  $u$  and  $u_t$  represent the output voltage of the Proportion Integral Differential (PID) closed-loop feedback controller and the voltage compensated after. As shown in Figure 3, the control method's structure includes a PID closed-loop feedback controller  $C_{PID}(s)$ , whose output voltage is compensated through frequency domain characteristics to form a control voltage used to regulate the system's mo-

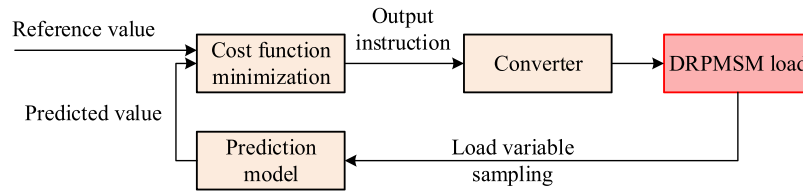


FIGURE 4. FS-MPC flow diagram.

tion. Building upon the PID closed-loop feedback controller, an element called fractional-order lead-lag compensator  $C_F(s)$  is introduced. Its role is to adjust amplitude and phase angle characteristics within the specified frequency domain range, enhancing the system's responsiveness to low-frequency signals. The specific expressions for  $C_{PID}(s)$  and  $C_F(s)$  are given by Equation (11).

$$\begin{cases} C_{PID}(s) = \frac{k_D s^2 + k_P s + k_I}{s} \\ C_F(s) = \frac{K(\lambda x s^a + 1)}{\lambda s^a + 1} \end{cases} \quad (11)$$

In Equation (11),  $k_D$ ,  $k_P$ ,  $k_I$  represent the differential gain, proportional gain, and integral gain, respectively.  $K$ ,  $\lambda$ ,  $x$  are parameters of the compensator, and  $a$  is the order of the compensator. In the feedback control system of the DRPMSM, the response to inputs is relatively weak at low frequencies, meaning that the closed-loop magnitude approaches zero. Simultaneously, the closed-loop error mainly exists in the low-frequency range, i.e., when the DRPMSM responds slowly to input signals, resulting in a significant error. In the low-frequency range, compensator parameters are determined by considering error variations to achieve precise control of the closed-loop magnitude characteristics. Therefore, based on this, the study explores the utilization of Finite Set Model Predictive Control (FS-MPC) to achieve predictive fault-tolerant control. In the context of DRPMSM, the core idea of FS-MPC is to select the optimal voltage vector for the system through the computation of a cost function to achieve high-precision and stable control. In FS-MPC, the switch control function of the inverter is crucial. The research employs a three-phase two-level inverter, which has a relatively simple circuit structure, making the design and implementation of the control function more intuitive and feasible. The FS-MPC flow diagram is shown in Figure 4.

From Figure 4, FS-MPC first collects the DRPMSM related variables through sensors, such as speed, current, and torque. Then the prediction model of DRPMSM is built, and the prediction model is brought into the cost function for calculation. The cost function considers the error between the predicted value and reference value of the system control variable. Then, the operating state of DRPMSM is adjusted as close as possible to the reference value by selecting the control action that minimizes the cost function. Finally, the optimal control action is input into the inverter, and the corresponding voltage vector is synthesized by the inverter and used in DRPMSM to achieve accurate control of its operating state and stability regulation. The specificity of the FS-MPC method is that by calculating the cost function, the method selects the optimal current vec-

tor to achieve the high precision and stability control of the DRPMSM system. The simplified three-phase two-level inverter structure can effectively reduce the complexity and loss of the inverter and improve the control efficiency. In addition, the FS-MPC method is based on the basic current vector control mode, and the output current vector of each cycle has the characteristic of fixed selection, which further improves the control efficiency of the system. The predictive model expression is shown in Equation (12).

$$\begin{cases} i_d(k+1) = i_d(k) + (-R_s i_d + \omega L_q i_q + u_d + \omega \psi_f) \frac{T_s}{L_d} \\ i_q(k+1) = i_q(k) + (-R_s i_q + \omega L_s i_s + u_d + \omega \psi_f) \frac{T_s}{L_q} \end{cases} \quad (12)$$

In Equation (12),  $T_s$  represents the sampling period, and  $k$  represents the sampling time. Thus,  $i_d(k+1)$  and  $i_q(k+1)$  represent the predicted currents, while  $i_d(k)$  and  $i_q(k)$  represent the current values at the present time. The study focuses on current fault-tolerant control for demagnetization faults in DRPMSM, emphasizing the minimization of the error between the current reference value and predicted current value to achieve better current fault-tolerant performance. The cost function  $J$  is defined as shown in Equation (13).

$$\begin{cases} J = |i'_d(k) - i_d(k+1)| + |i'_q(k) - i_q(k+1)| \\ s.t. V_n \in \{V_0, V_1, \dots, V_7\} \end{cases} \quad (13)$$

In Equation (13),  $i'_d(k)$  and  $i'_q(k)$  represent the reference currents, and  $V_0, V_1, \dots, V_7$  represent the voltage space vector values corresponding to the eight switch states of the three-phase two-level inverter.  $V_n$  satisfies Equation (14).

$$V_n = \frac{2V_{dc}}{3} \left[ S_a^k + e^{j\frac{2\pi}{3}} S_b^k + e^{j\frac{4\pi}{3}} S_c^k \right] \quad (14)$$

In Equation (14),  $V_{dc}$  represents the DC bus voltage of the inverter, and  $S_a^k, S_b^k, S_c^k$  represent the switch functions of the inverter at the  $k$ th sampling instant. Each of the eight switching states of the three-phase two-level inverter corresponds to a unique voltage vector. In each sampling period, the voltage vectors of these eight switch states are input into the model predictive equation, obtaining predicted values for eight control variables. These predicted values are compared one by one with the respective reference values through the cost function. The voltage vector that minimizes the cost function, along with its corresponding switch state function, is input into the inverter,

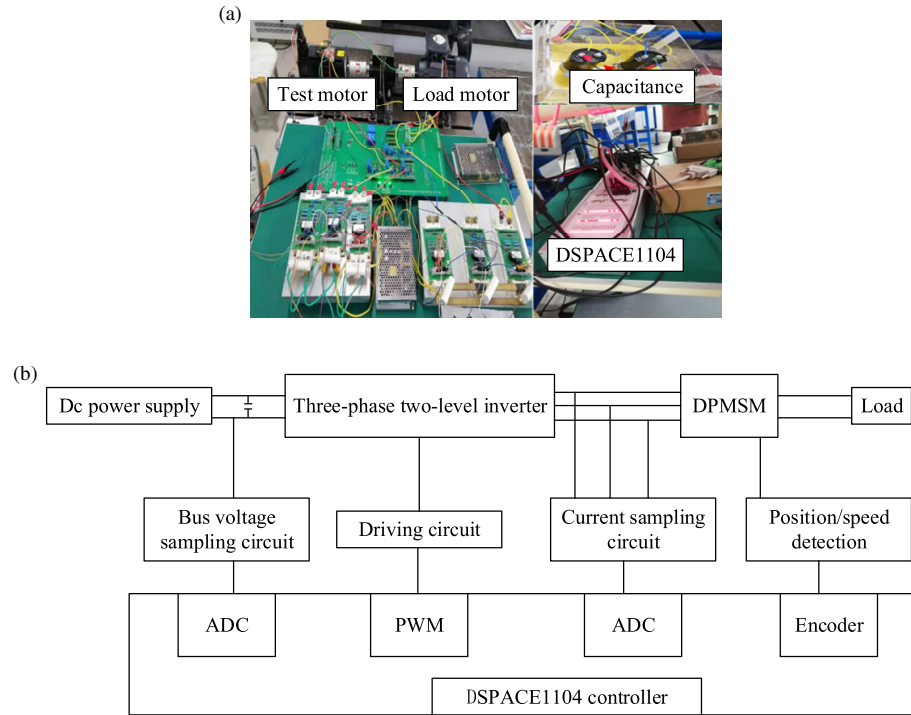


**FIGURE 5.** Experimental hardware platform construction. (a) Hardware diagram. (b) Component connection block diagram.

generating the corresponding voltage vector, which is then applied to the DRPMSM. This process is designed in the study to enable the actual current of the motor to closely follow the reference current, ensuring stable motor operation. The study achieves predictive fault-tolerant control by dynamically adjusting inverter output, enhancing the system's adaptability to load variations, and enabling the motor to better cope with demagnetization faults.

#### 4. EXPERIMENTAL VERIFICATION AND ANALYSIS OF FAULT-TOLERANT CONTROL FOR DRPMSM WITH CLOSED-LOOP IDENTIFICATION

The performance of the closed-loop identification model for DRPMSM was validated. The process included experiments for parameter identification, simulation experiments for different parameters, and open-loop versus closed-loop comparison experiments. Subsequently, the performance of fault-tolerant control for DRPMSM was also verified.

##### 4.1. Performance Verification and Analysis of the Closed-Loop Identification Model

To verify the effectiveness and superiority of the closed-loop identification model, extensive experiments were conducted. The study involved collecting motion information of DRPMSM on a gantry motion platform and controlling DRPMSM using the DSPACE1104 controller. The establishment of the experimental hardware platform is shown in Figure 5.

Initially, parameter identification experiments were conducted, followed by a comparison between the open-loop

identification model and closed-loop identification model. The results are depicted in Figure 6.

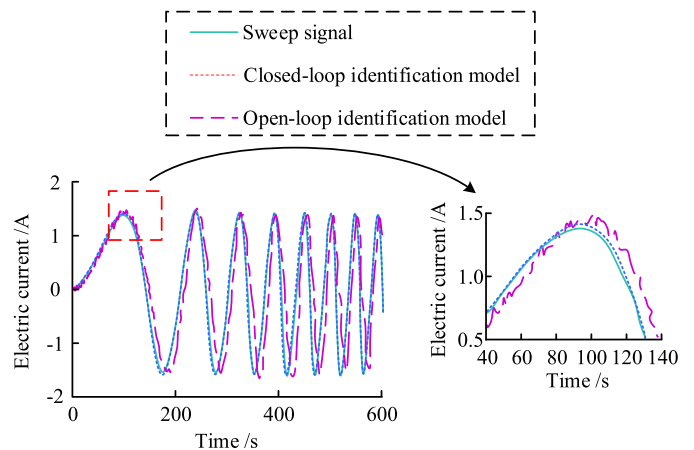


**FIGURE 6.** Parameter identification experiment and open-loop comparison.

From Figure 6, it could be observed that under the open-loop identification model, the measured current values exhibited varying degrees of displacement and amplitude changes compared to the sweep signal throughout the measurement period. In contrast, under the closed-loop identification model, the measured current values showed small errors compared to the sweep signal, with high tracking accuracy. Moreover, the closed-loop identification model effectively suppressed subtle fluctuations in current, enhancing the accuracy of parameter identification. Consequently, the study used these results to calculate the parameter values in Equation (10), specifically,

**TABLE 1.** Comparison results of following difference at different frequencies.

Frequency	Method and comparison	Error		
		MAX	MAE	RMSE
2 Hz	PID method ( $\mu\text{m}$ )	195.54	115.38	122.74
	Research method ( $\mu\text{m}$ )	42.34	14.52	16.14
	Error reduction degree (%)	78.34	87.41	86.85
5 Hz	PID method ( $\mu\text{m}$ )	348.17	153.82	194.82
	Research method ( $\mu\text{m}$ )	106.48	26.94	30.14
	Error reduction degree (%)	69.41	82.48	84.52
10 Hz	PID method ( $\mu\text{m}$ )	694.61	199.74	302.36
	Research method ( $\mu\text{m}$ )	231.52	27.15	49.27
	Error reduction degree (%)	66.66	86.40	83.70

**TABLE 2.** Simulation of DRPMSM parameters and experimental conditions.

Motor parameter	Numerical value	Experimental condition	Numerical value
Dc-side bus voltage	1500 V	Limit value of stator current	200 A
Stator winding phase resistance	0.02 $\Omega$	Reference speed	200 rad/s
Number of poles	4	Load torque	300 N
Stator winding $D$ -axis inductance	0.001 H	Simulation time	8 s
Stator winding $Q$ -axis inductance	0.003572 H	Amplitude change	0.892 Wb $\rightarrow$ 0.4 Wb
Rotor flux	0.892 Wb	Magnetic declination change	0 rad $\rightarrow$ $\pi/6$ rad
Moment of inertia	100 kg·m <sup>2</sup>	Time point of magnetic failure	4 s

$b_2'' = 5.389$ ,  $b_1'' = 52.25$ ,  $b_0'' = 8.6$ ,  $a_3'' = 1$ ,  $a_2'' = 7.72$ ,  $a_1'' = 25.47$ , and  $a_0'' = 9.341$ . Building upon this, the study conducted simulation experiments on the parameters and orders of the fractional-order lead-lag compensator component in the closed-loop identification model. The results are illustrated in Figure 7.

Figures 7(a), (b), (c), and (d) respectively illustrate the frequency domain characteristics of the compensator under different parameter values. Combining these figures, it could be observed that the fractional-order lead-lag compensator could adjust the amplitude and phase of the system within specific frequency ranges. It exhibited a range of applicability, providing effective adjustments not only for low-frequency signals but also demonstrating good adaptability to high-frequency signals. The phase characteristics manifested adjustments only at specified angular frequencies and their surrounding frequency domains, without affecting the entire frequency spectrum. By appropriately adjusting the order, the system remained insensitive to high-frequency noise, maintained a suitable bandwidth for rapid response to normal signal variations, and could adjust the system's frequency response. The introduction of the fractional-order lead-lag compensator contributed to improving the system's frequency domain characteristics, enhancing the control system's responsiveness to both low- and high-frequency signals. Furthermore, the proposed feedback control method and PID feedback control method were compared

under sinusoidal motions at 2 Hz, 5 Hz, and 10 Hz. Follow-up errors were calculated, and the results are presented in Table 1.

The sinusoidal motion amplitude in Table 1 was 10 mm. It can be observed from Table 2 that at a frequency of 2 Hz, the PID feedback control method had maximum, average absolute, and root mean square errors of 195.54  $\mu\text{m}$ , 115.38  $\mu\text{m}$ , and 122.74  $\mu\text{m}$ , respectively. In contrast, the proposed feedback control method performed relatively better at 2 Hz, with maximum, average absolute, and root mean square errors of 42.34  $\mu\text{m}$ , 14.52  $\mu\text{m}$ , and 16.14  $\mu\text{m}$ , respectively. The reduction in follow-up errors for the proposed method compared to PID at 2 Hz was significant, with percentage decreases of 78.34%, 87.41%, and 86.85%, respectively. Similarly, at frequencies of 5 Hz and 10 Hz, the follow-up errors of the proposed feedback control method remained significantly lower than those of the PID feedback control method. This indicates that with the assistance of the closed-loop identification model, the follow-up errors of DRPMSM were markedly reduced.

#### 4.2. Simulation Experiment and Practical Application Analysis of DRPMSM Predictive Fault-Tolerant Control

Furthermore, to verify the effectiveness and superiority of the predictive fault-tolerant control method proposed based on the combined transformation identification model, the study utilized MATLAB software for the simulation modeling of the closed-loop identification model and DRPMSM, conducting

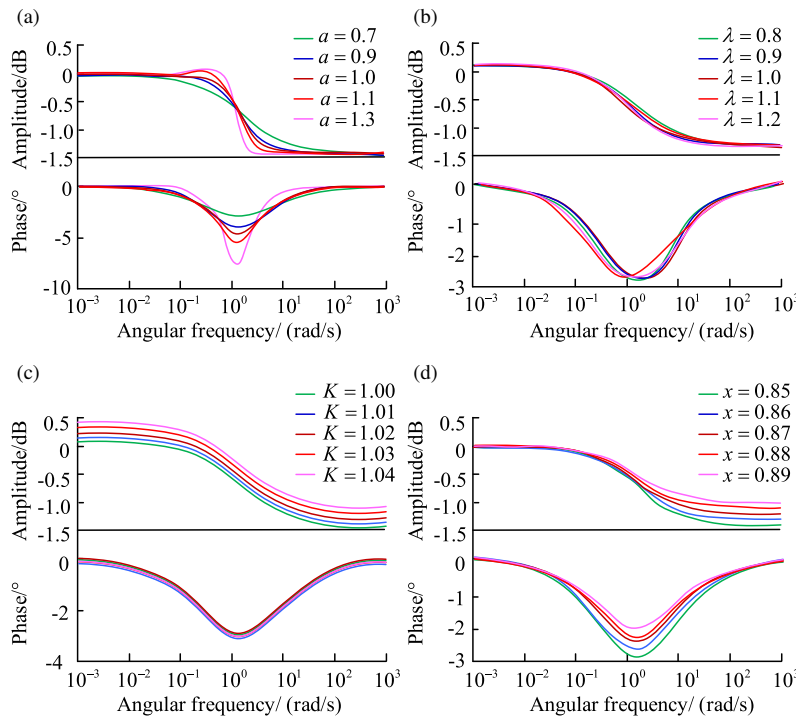


**FIGURE 7.** Simulation experiments of fractional lead-lag compensator components. (a)  $\lambda = 0.8$ ,  $K = 1.00$ ,  $x = 0.85$ . (b)  $a = 0.7$ ,  $K = 1.00$ ,  $x = 0.85$ . (c)  $a = 0.7$ ,  $\lambda = 0.8$ ,  $x = 0.85$ . (d)  $a = 0.7$ ,  $\lambda = 0.8$ ,  $K = 1.00$ .

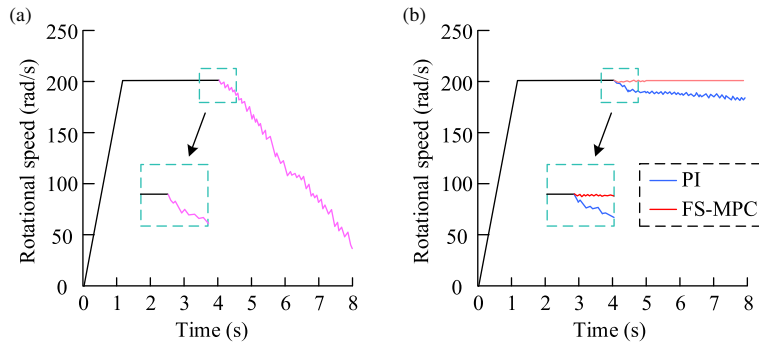


**FIGURE 8.** Comparison of fault-tolerant control results in speed simulation experiments. (a) Before and after the magnetic failure. (b) Comparison of PI and FS-MPC.

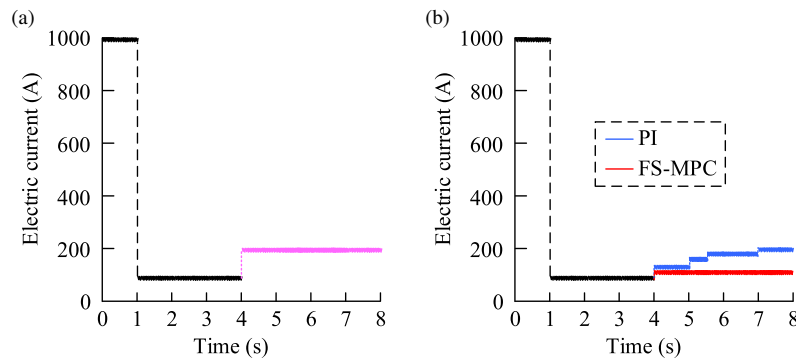
simulation experiments. The simulation parameters for the constructed DRPMSM in the study are detailed in Table 2.

Table 2 provides a comprehensive presentation of DRPMSM parameters and experimental conditions. The study compared the effects of traditional PI fault-tolerant control inherent in DRPMSM with the proposed FS-MPC fault-tolerant control before and after the occurrence of demagnetization faults in DRPMSM. Firstly, the simulation of DRPMSM speed was conducted. The results are depicted in Figure 8.

As evident from Figure 8(a), approximately 1 s after the initiation of DRPMSM, it reached the reference speed of 200 rad/s. However, after a demagnetization fault occurred around the 4th second, the speed rapidly decreased, reaching only 38.24 rad/s at the end of the 8 s simulation. Figure 8(b) shows that under PI fault-tolerant control, the speed declined within 0.5 s after the demagnetization fault at a decreasing rate, stabilizing

above 180 rad/s subsequently. On the other hand, under FS-MPC fault-tolerant control, the speed exhibited minor fluctuations within the initial 0.5 s after the fault and then stabilized at 200 rad/s. Subsequently, the study simulated the current of DRPMSM, and the results are illustrated in Figure 9.

In Figure 9(a), after a demagnetization fault occurred around the 4th second, the current directly reached the rated current of 200 A set by the three-phase two-level inverter. Figure 9(b) shows that for PI fault-tolerant control, the current, although maintained within the rated current after the fault, exhibited fluctuations at the 7th second, reaching 200 A. In contrast, under FS-MPC fault-tolerant control, the current underwent changes after the demagnetization fault but remained below the rated current of 200 A, maintaining stability. Furthermore, the study simulated the torque variation of DRPMSM, and the results are presented in Figure 10.



**FIGURE 9.** Comparison of fault-tolerant control results in current simulation experiments. (a) Before and after the magnetic failure. (b) Comparison of PI and FS-MPC.

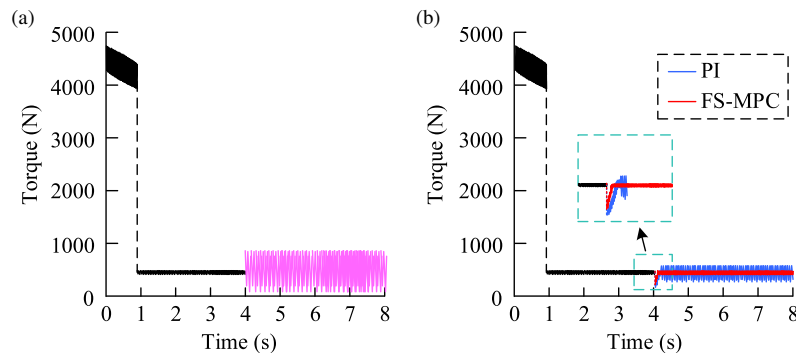


**FIGURE 10.** Comparison of fault-tolerant control results in torque simulation experiments. (a) Before and after the magnetic failure. (b) Comparison of PI and FS-MPC.

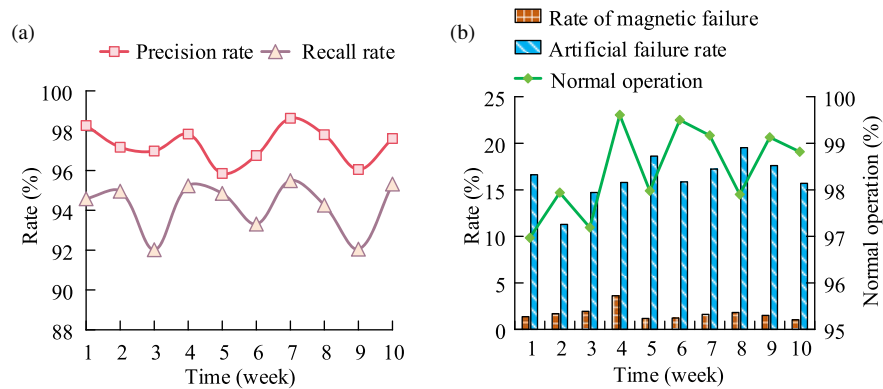


**FIGURE 11.** Comparison of fault-tolerant control results in torque simulation experiments. (a) Working condition detection. (b) Fault tolerant control results.

Figure 10(a) illustrates that after a demagnetization fault occurred around the 4th second, the torque of DRPMSM no longer remained balanced and experienced significant fluctuations, rendering DRPMSM unable to operate normally. Figure 10(b) indicates that PI fault-tolerant control resulted in a sudden drop in torque after the 4th second of the demagnetization fault, recovering to normal levels after approximately 0.2 s, with minor fluctuations near the original torque, remaining unstable. In contrast, FS-MPC fault-tolerant control restored the torque to its original value within 0.1 s after the demagnetization fault and maintained a constant torque, enabling normal operation of DRPMSM. Finally, on the basis of the simulation experiment, the daily work of the simulated DRPMSM within

10 weeks was studied, and the 10-week loss was set at 3.00%, with the weekly loss floating no more than 0.05% on the basis of the average value of 0.30%. At the same time, the working state of DRPMSM during the simulation period was recorded. The results are shown in Figure 11.

Figure 11(a) indicates that within 10 weeks of implementation, the operational accuracy of DRPMSM reached 95%–99%, averaging 97.10%. Considering positive cases as situations requiring fault tolerance when faults occurred, the recall rate reached 92%–96%, averaging 94.26%. Figure 11(b) reveals that the natural occurrence probability of demagnetization faults in DRPMSM generally ranged from 1% to 2%, with only the 4th week showing 3.61%. Therefore, the study in-

roduced randomly added artificially induced demagnetization faults of 10%–20%. Despite the faults, an average of 97.69% of DRPMSM continued to operate normally, validating the effectiveness and practicality of predictive fault-tolerant control.

## 5. CONCLUSION

In response to the increased demand for higher precision in motor systems due to the rapid development of industry, a study was conducted focusing on the DRPMSM. A closed-loop identification model was designed, and its mathematical model and closed-loop transfer function expression were established. Building upon this foundation, feedback control and predictive fault-tolerant control were proposed. The research content was subjected to simulation experiments to validate the effectiveness of the study. Experimental verification on a gantry motion platform confirmed that the closed-loop identification model exhibited higher tracking accuracy in DRPMSM current measurement than the open-loop model. The fractional-order lead-lag compensator successfully adjusted the system's frequency domain characteristics under different parameters. The feedback control method introduced in the study demonstrated smaller tracking errors. For instance, at a frequency of 2 Hz, the maximum, average absolute, and root mean square errors were 42.34  $\mu\text{m}$ , 14.52  $\mu\text{m}$ , and 16.14  $\mu\text{m}$ , respectively. This showed a significant reduction in tracking errors compared to the PID feedback control method at 2 Hz, with percentage reductions of 78.34%, 87.41%, and 86.85%, respectively. Concerning predictive fault-tolerant control, under FS-MPC fault-tolerant control, slight speed fluctuations occurred within 0.5 s after a demagnetization fault. The speed stabilized at 200 rad/s, and the current, although varying, remained below the rated current of 200 A, which was stable. The torque recovered to its original value within 0.1 s after the demagnetization fault and remained constant. In the event of a demagnetization fault, an average of 97.69% of DRPMSM continued to operate normally. Overall, the closed-loop identification model and predictive fault-tolerant control methods demonstrated significant advantages in enhancing DRPMSM performance and mitigating the impact of demagnetization faults on the system. This provides strong support for the stable operation of DRPMSM in practical applications. Furthermore, the study did not address other faults in DRPMSM, leaving room for further refinement of methods and experiments in subsequent research.

## REFERENCES

- [1] Jensen, K. T., N. K. Harpaz, A. K. Dhawale, S. B. E. Wolff, and B. P. Ólveczky, "Long-term stability of single neuron activity in the motor system," *Nature Neuroscience*, Vol. 25, No. 12, 1664–1674, 2022.
- [2] Błaszczyk, J. W., A. Fredyk, P. M. Błaszczyk, and M. Ashtiani, "Step response of human motor system as a measure of postural stability in children," *IEEE Transactions on Neural Systems and Rehabilitation Engineering*, Vol. 28, No. 4, 895–903, 2020.
- [3] Thanh, P. T., T. X. Tinh, D. P. Nam, D. S. Luat, and N. H. Quang, "On finite-time output feedback sliding mode control of an elastic multi-motor system," *International Journal of Power Electronics and Drive System (IJPEDS)*, Vol. 12, No. 1, 10–19, 2021.
- [4] Wellendorf, A., P. Tichelmann, and J. Uhl, "Performance analysis of a dynamic test bench based on a linear direct drive," *Archives of Advanced Engineering Science*, Vol. 1, No. 1, 55–62, 2023.
- [5] Cannon, J. J. and A. D. Patel, "How beat perception co-opts motor neurophysiology," *Trends in Cognitive Sciences*, Vol. 25, No. 2, 137–150, 2021.
- [6] Peng, S., G. Zhang, Z. Zhou, X. Gu, and C. Xia, "MPTC of NP-clamped three-level inverter-fed permanent-magnet synchronous motor system for NP potential imbalance suppression," *IET Electric Power Applications*, Vol. 14, No. 4, 658–667, 2020.
- [7] Yan, B., Y. Yang, and X. Wang, "Design of a large capacity line-start permanent magnet synchronous motor equipped with hybrid salient rotor," *IEEE Transactions on Industrial Electronics*, Vol. 68, No. 8, 6662–6671, 2020.
- [8] Ladghem-Chikouche, B., K. Boughrara, F. Dubas, L. Roubache, and R. Ibtouen, "Semi-analytical magnetic field calculation for dual-rotor permanent-magnet synchronous machines by using hybrid model," *IEEE Transactions on Magnetics*, Vol. 58, No. 1, 1–10, 2021.
- [9] Wu, J., Y. Hu, B. Zhang, G. Feng, and Z. Liu, "Comparison and analysis of different rotor structures of double-stator permanent magnet synchronous motor," *IET Electric Power Applications*, Vol. 16, No. 6, 685–700, 2022.
- [10] Ghaffarpour, A. and M. Mirsalim, "Split-tooth double-rotor permanent magnet switched reluctance motor," *IEEE Transactions on Transportation Electrification*, Vol. 8, No. 2, 2400–2411, 2022.
- [11] Allahyari, A. and H. Torkaman, "A novel high-performance consequent pole dual rotor permanent magnet vernier machine," *IEEE Transactions on Energy Conversion*, Vol. 35, No. 3, 1238–1246, 2020.
- [12] Sun, X., Z. Jin, Y. Cai, Z. Yang, and L. Chen, "Grey wolf optimization algorithm based state feedback control for a bearingless permanent magnet synchronous machine," *IEEE Transactions on Power Electronics*, Vol. 35, No. 12, 13 631–13 640, 2020.
- [13] Fang, S., Y. Wang, W. Wang, Y. Chen, and Y. Chen, "Design of permanent magnet synchronous motor servo system based on improved particle swarm optimization," *IEEE Transactions on Power Electronics*, Vol. 37, No. 5, 5833–5846, 2021.
- [14] Zuo, Y., X. Zhu, X. Si, and C. H. T. Lee, "Fault-tolerant control for multiple open-leg faults in open-end winding permanent magnet synchronous motor system based on winding reconnection," *IEEE Transactions on Power Electronics*, Vol. 36, No. 5, 6068–6078, 2020.
- [15] Jlassi, I. and A. J. M. Cardoso, "Open-circuit fault-tolerant operation of permanent magnet synchronous generator drives for wind turbine systems using a computationally efficient model predictive current control," *IET Electric Power Applications*, Vol. 15, No. 7, 837–846, 2021.
- [16] Ugale, R. T. and B. N. Chaudhari, "Performance enhancement of line start permanent magnet synchronous motor with a special consequent pole rotor," *IEEE Transactions on Energy Conversion*, Vol. 36, No. 3, 1972–1982, 2020.
- [17] Deng, W., S. Zuo, W. Chen, Z. Qian, C. Qian, and W. Cao, "Comparison of eccentricity impact on electromagnetic forces in internal-and external-rotor permanent magnet synchronous motors," *IEEE Transactions on Transportation Electrification*, Vol. 8, No. 1, 1242–1254, 2021.
- [18] Zhao, H., C. Liu, Z. Song, and S. Liu, "Design and control of a new compound double-rotor electric machine for hybrid propulsion system," *IEEE Transactions on Power Electronics*, Vol. 37, No. 3, 3283–3296, 2021.